

Figure 3 shows numerical results and the experimental estimates for the amplitude and phase of the horizontal and vertical wave-coherent wind velocities versus  $c$  at fixed  $z$  and  $u_*$ . For the numerical  $\tilde{w}(z, c|u_*)$  at constant  $z$  and  $u_*$  the abrupt change of its phase is clearly recognizable (Fig. 3d), occurring at  $c = U(z_i)$ ,  $z_i$  being the vertical position of the instrument. Indeed, for the wave mode  $c = U(z_i)$  the instrument is at the mode's critical height; for all the slower modes  $c < U(z_i)$  the instrument is above their critical heights ( $z_i > z_c$ ), and for all faster modes  $c > U(z_i)$  the instrument is below their critical heights ( $z_i < z_c$ ). The numerical and the experimental results seem to agree closely and the distinct wave-induced flow features, such as the abrupt change of the phase and the minimum of the amplitude about  $c = U(z_i)$ , are clearly captured by the experimental data. Nonlinear interaction between wave modes transfers most of the wave energy to the long (fast) waves and leaves little energy in the short (slow) modes, as illustrated by the wave spectrum  $S_{\eta\eta}(c)$  in Fig. 3e. Also, as the wave-induced field's vertical decay is scaled by the wavelength, at a given height  $z_i$  the shorter the wave the stronger the attenuation of the velocity induced by the wave. In combination, these two circumstances result in a low signal-to-noise ratio for the short-wave signature in the wind and greater uncertainty for the estimated amplitude and phase of the velocity induced by these short (slow) waves. Therefore, numerics and experiment show closer agreement for long (fast) waves and greater divergence for short (slow) waves (Fig. 3a–d).

Throughout the experiment the wave-induced flow maintains the critical layer pattern. That pattern is clearly observed in the phase of the vertical wave-induced velocity fluctuations (Fig. 4), which exhibits a distinct and persistent change along the mean wind line  $c = U(z_i)$ . For fast ( $c > U(z_i)$ ) waves the phase remains close to  $90^\circ$ , while for waves slower than the mean wind ( $c < U(z_i)$ ) it rapidly decreases, as predicted by the numerical results in Figs 1d and 3d.

Thus we identified the wave-induced flow from field measurements and showed that its configuration is closely consistent with the predictions of the critical-layer theory<sup>3</sup> for the range  $16 < c/u_* < 40$ . Such a result confirms that for the resolved wave scales the critical-layer mechanism of wind–wave coupling is clearly active over the open ocean. Models of climate as well as weather and wave forecasting<sup>19</sup> rely on current knowledge about air–sea fluxes as boundary conditions on the ocean–atmosphere interface. Data from measurements have been used in extensive efforts to parameterize the air–sea momentum flux by expressing the ocean surface drag coefficient  $C_D = u_*^2/U^2$  through a single variable. There, the experimental points have systematically failed to collapse onto a particular curve<sup>10–12</sup> and the observed scatter has not been reduced by accumulating more statistics and by improving the quality of measurements. The evidence presented here in support of the critical layer mechanism<sup>3</sup> indicates (i) that the total wave-induced momentum flux  $\tilde{\tau} \equiv -\rho\langle\tilde{u}\tilde{w}\rangle = \tilde{E}/c$  is controlled by the wave spectrum and not by a single representative parameter and (ii) that  $\tilde{\tau}$  has a considerable vertical variability. These two circumstances are probably major contributors to the observed scatter of drag coefficient estimates. □

Received 24 May; accepted 17 December 2002; doi:10.1038/nature01382.

1. Thomson, W. (Lord Kelvin) Hydrokinetic solutions and observations. *Phil. Mag.* 42(4), 362–377 (1871); *Math Phys. Pap.* 4, 80.
2. Jeffreys, H. On formation of waves by wind. *Proc. R. Soc. Lond. A* 107, 189–206 (1924).
3. Miles, J. W. On the generation of surface waves by shear flows. *J. Fluid Mech.* 3, 185–204 (1957).
4. Belcher, S. & Hunt, J. C. R. Turbulent shear flow over slowly moving waves. *J. Fluid Mech.* 251, 109–148 (1993).
5. Meirink, J. F. & Makin, V. Modelling low-Reynolds-number effects in the turbulent air flow over water waves. *J. Fluid Mech.* 415, 155–174 (2000).
6. Li, P. Y., Xu, D. & Taylor, P. A. Second order turbulence closure modeling for air flow over water waves. *Boundary-Layer Meteorol.* 95, 397–425 (2000).
7. Sullivan, P., McWilliams, J. & Moeng, C.-H. Simulation of turbulent flow over idealized water waves. *J. Fluid Mech.* 404, 47–85 (2000).
8. Hristov, T., Friehe, C. & Miller, S. Wave-coherent fields in air flow over ocean waves: Identification of cooperative behavior buried in turbulence. *Phys. Rev. Lett.* 81, 5245–5248 (1998).

9. Phillips, O. M. On the generation of waves by turbulent wind. *J. Fluid Mech.* 2, 417–445 (1957).
10. Donelan, M. *Air–Sea Interaction* Vol. 9 (eds LeMehaute, B. & Hanes, D. M.) 239–292 (John Wiley & Sons, New York, 1990).
11. Komen, G., Cavaleri, L., Donelan, M., Hasselmann, K., Hasselmann, S. & Janssen, P. *Dynamics and Modelling of Ocean Waves* (Cambridge Univ. Press, Cambridge, 1994).
12. Csanady, G. T. *Air–Sea Interaction: Laws and Mechanisms* (Cambridge Univ. Press, Cambridge, 2001).
13. Longuet-Higgins, M. S. Action of variable stress at the surface of water waves. *Phys. Fluids* 12, 737–740 (1969).
14. Davis, R. E. On the turbulent flow over a wavy boundary. *J. Fluid Mech.* 42, 721–731 (1970).
15. Landau, L. D. & Lifshitz, E. M. *Fluid Mechanics* 172–176 (Pergamon, Oxford, 1986).
16. Lin, C. *The Theory of Hydrodynamic Stability* (Cambridge Univ. Press, Cambridge, 1955).
17. Phillips, O. M. *The Dynamics of the Upper Ocean* 108 (Cambridge Univ. Press, Cambridge, 1977).
18. Hasse, L. & Dobson, F. *Introductory Physics of the Atmosphere and Ocean* 101 (D. Reidel, Boston, 1986).
19. Janssen, P. et al. *Impact and Feedback of Ocean Waves on the Atmosphere* Vol. 1 of *Advances in Fluid Mechanics* Ch. 5 155–198 (WIT, Ashurst, 2002).

**Acknowledgements** J. Edson's help and the expert assistance of FLIP's captain Tom Golfinos and crew made it possible to carry out the experiment. In discussions, comments or criticisms came from O. Phillips, M. Donelan, J. McWilliams, P. Sullivan, J.C.R. Hunt, P. Taylor, M. McIntyre, S. Belcher, V. Makin and V. Kudryavtsev. ONR (Marine Meteorology) has provided the funding for this work.

**Competing interests statement** The authors declare that they have no competing financial interests.

**Correspondence** and requests for materials should be addressed to T.S.H. (e-mail: Tihomir.Hristov@jhu.edu).

## Iron–silica interaction at extreme conditions and the electrically conducting layer at the base of Earth's mantle

L. Dubrovinsky\*, N. Dubrovinskaia\*, F. Langenhorst\*, D. Dobson\*, D. Rubie†, C. Gebmann†, I. A. Abrikosov‡, B. Johansson‡§, V. I. Baykov§, L. Vitos☆, T. Le Bihan¶, W. A. Crichton¶, V. Dmitriev# & H.-P. Weber#

\* Bayerisches Geoinstitut, Universität Bayreuth, D-95440 Bayreuth, Germany  
 † Max-Planck-Institut für Chemie, Joh.-Joachim-Becher-Weg 27, 0-55128 Mainz, Germany  
 ‡ Condensed Matter Theory Group, Department of Physics, Uppsala University, S-751 21 Uppsala, Sweden  
 § Applied Materials Physics, Department of Materials Science and Engineering, Royal Institute of Technology, Brinellvägen 23, SE-100 44, Stockholm, Sweden  
 ¶ Theoretical Physics Department, Moscow State Institute of Steel and Alloys, Leninskii pr., 4, 117936 Moscow, Russia  
 ¶ European Synchrotron Radiation Facility,  
 # Swiss-Norwegian Beam Lines at ESRF, F-38043 Grenoble, France  
 ☆ Research Institute for Solid State Physics and Optics, H-1525 Budapest, P.O. Box 49, Hungary

The boundary between the Earth's metallic core and its silicate mantle is characterized by strong lateral heterogeneity and sharp changes in density, seismic wave velocities, electrical conductivity and chemical composition<sup>1–7</sup>. To investigate the composition and properties of the lowermost mantle, an understanding of the chemical reactions that take place between liquid iron and the complex Mg-Fe-Si-Al-oxides of the Earth's lower mantle is first required<sup>8–15</sup>. Here we present a study of the interaction between iron and silica (SiO<sub>2</sub>) in electrically and laser-heated diamond anvil cells. In a multianvil apparatus at pressures up to 140 GPa and temperatures over 3,800 K we simulate conditions down to the core–mantle boundary. At high temperature and pressures below 40 GPa, iron and silica react to form iron oxide and an iron–silicon alloy, with up to 5 wt% silicon. At pressures

of 85–140 GPa, however, iron and SiO<sub>2</sub> do not react and iron–silicon alloys dissociate into almost pure iron and a CsCl-structured (B2) FeSi compound. Our experiments suggest that a metallic silicon-rich B2 phase, produced at the core–mantle boundary (owing to reactions between iron and silicate<sup>2,9,10,13</sup>), could accumulate at the boundary between the mantle and core and explain the anomalously high electrical conductivity of this region<sup>6</sup>.

Although iron (with ~5 wt% Ni) is a dominant component of the Earth's core, Fe–Ni alloy is too dense by ~10% for the outer liquid core and by 2–5% for solid inner core to satisfy the observed density along any reasonable geotherm<sup>16</sup>. Thus, on the basis of cosmochemistry, it has been proposed that the core also contains one or more light elements, such as H, C, O, S, and/or Si<sup>17</sup>. It is likely that such light elements were dissolved into the liquid metal during core formation in a magma ocean<sup>8</sup> during the early history of the Earth. At the probable temperature of the magma ocean (~2,800 K), 2–6 wt% Si can dissolve in liquid Fe at 25 GPa and an appropriate oxygen fugacity<sup>8</sup>. On the basis of a simple thermodynamic model, it was proposed that the solubility of Si at core conditions is close to zero<sup>8</sup>. Thus, after core formation, Si should be expelled from liquid Fe as the metallic core evolves towards chemical equilibrium. In particular, it was demonstrated<sup>18</sup> that

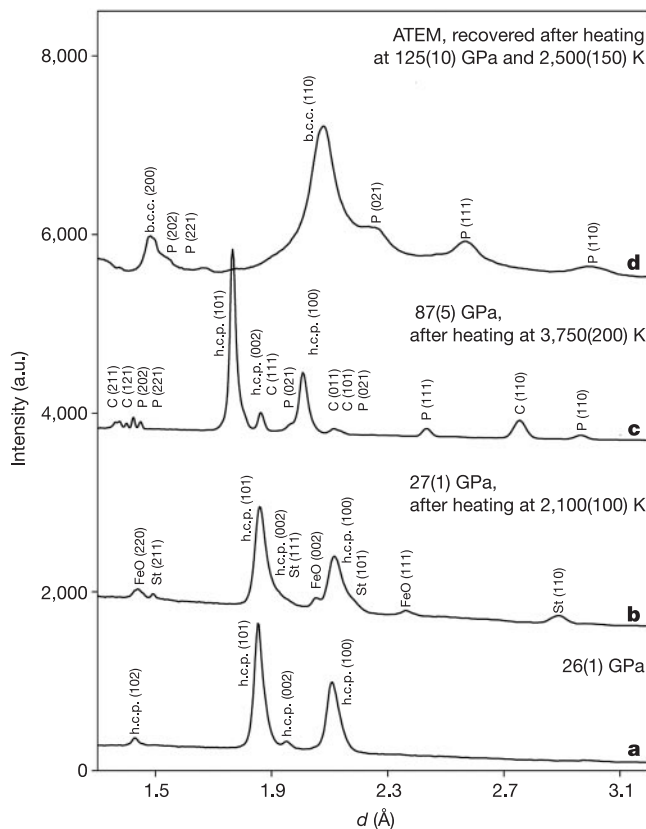


**Figure 1** Representative spectra obtained in experiments with iron and amorphous silica as starting materials. **a–c**, Angle-dispersive X-ray and **d**, electron diffraction patterns. **a**, At 26(1) GPa (where 26(1) represents 26 ± 1) before heating of the sample, only diffraction lines of ε-Fe (marked as h.c.p.) are present. **b**, After heating at 2,100(100) K silica crystallized in stishovite (St) and new lines of wüstite (FeO) appeared. **c**, Heating of iron and amorphous SiO<sub>2</sub> mixture at 85(5) GPa and 2,400(150) K resulted in crystallization of silica phases only (CaCl<sub>2</sub>- and α-PbO<sub>2</sub>-structures, marked (C) and (P), correspondingly), but wüstite was absent. **d**, Selected area electron diffraction spectrum of the material recovered after heating at 125(10) GPa and 2,500(150) K shows only the presence of α-PbO<sub>2</sub>-type (P) silica phase and iron (b.c.c.). ATEM, analytical transmission electron microscopy; h.c.p., hexagonal close packed; b.c.c., body-centred cubic.

iron can react with MgSiO<sub>3</sub>-perovskite at high pressures and temperatures. The chemical nature of this process is reduction of silicon by more electropositive iron with formation of iron oxide and iron silicide<sup>18</sup>.

Two important observations regarding high-pressure phase relations in this Fe–Si system have recently been reported: the synthesis of iron silicide with the CsCl (B2) structure at 24 GPa and high temperatures<sup>19</sup>, and the stabilization of the body-centred cubic (b.c.c.) structure in iron-rich Fe–Si alloys at pressures over 80 GPa and temperatures up to 2,400 K (ref. 17). In the light of these recent discoveries, we have further examined chemical reactions between Fe and SiO<sub>2</sub> at conditions of the Earth's mantle down to the core–mantle boundary (CMB).

We conducted three experiments in a multi-anvil apparatus (see Supplementary Information) on a mixture of Fe and SiO<sub>2</sub>, contained in MgO capsules, at 22 GPa and 2,473 K. Electron microprobe analysis shows that the products of all experiments are similar and consist of Fe–Si alloy with compositions ranging from 3.5 to 4.9 wt% Si, magnesiowüstite (a reaction product of the MgO capsule material), and (Mg,Fe)<sub>2</sub>SiO<sub>4</sub> (found at the capsule–sample

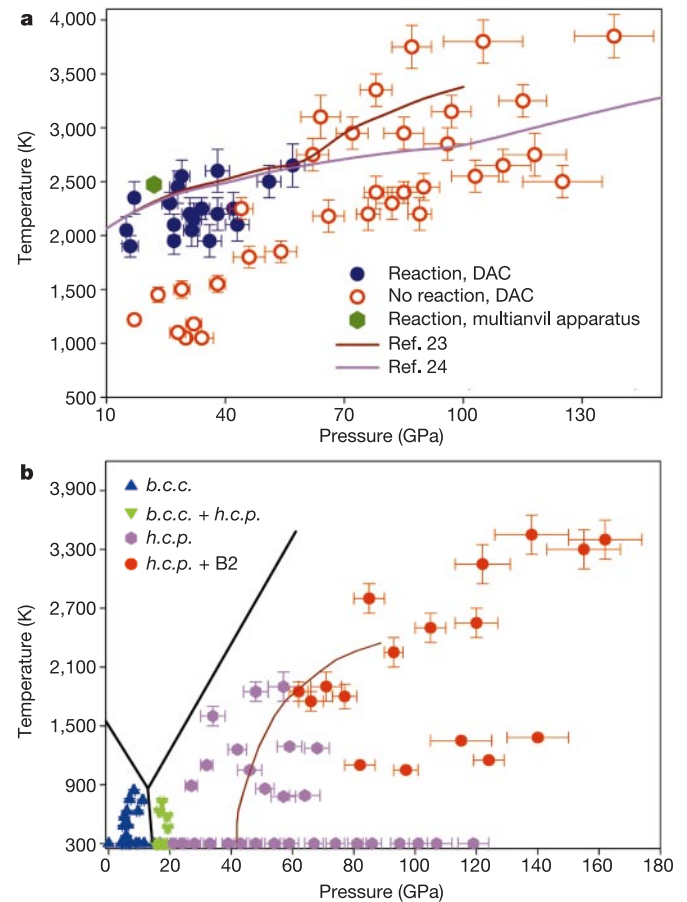


**Figure 2** Experimental results on the chemical interaction of iron and silica and behaviour of Fe–Si alloys at high pressures and temperatures. **a**, Filled blue dots show pressure and temperature conditions at which the reaction between iron and silica was observed, and open red circles show conditions at which the reaction does not occur. The green hexagon corresponds to observation of the reaction in multi-anvil experiments. Solid lines show melting curve of iron in pink<sup>23</sup> and dark red<sup>24</sup>. **b**, Phases observed in electrically-heated (below 1,500 K) and laser-heated (above 1,500 K) diamond anvil cell (DAC) experiments with iron–silicon alloys: 9.6(1), 5.1(1), 4.3(4) wt% Si. We found that all alloys behave similarly and symbols show only phase relations. Continuous black lines show phase relations in pure iron. The red curve shows a phase boundary between h.c.p. and h.c.p. + b.c.c. regions in a Fe–7.9 wt% Si alloy<sup>17</sup>.

interface). A sample reacted at high pressure and temperature for 90 min contains a very homogeneous 4.3(4) wt% Si (where 4.3(4) represents  $4.3 \pm 0.4$ ; average of 30 data points) metallic portion that is  $\sim 0.5$  mm in diameter. The Fe-Si alloy from this experiment was used in subsequent higher-pressure experiments using the diamond anvil cell (DAC) as described below.

The reaction between iron and silica was also studied *in situ* in the DAC. Iron foil, 5  $\mu$ m thick, was sandwiched between two layers of amorphous silica, compressed to high pressures and laser-heated from both sides. Amorphous silica was chosen to increase the reactivity of the oxide. Figure 1 shows representative angle-dispersive X-ray diffraction patterns. At 26(1) GPa and before

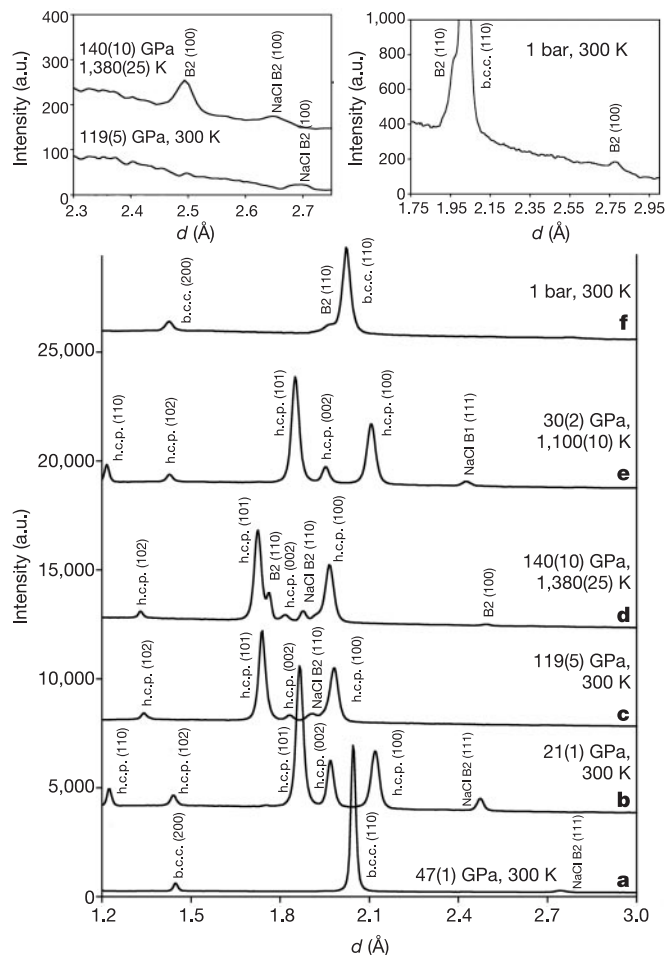


**Figure 3** Examples of X-ray diffraction patterns collected in experiments with Fe-5.1 wt% Si. **a**, At 4.7(1) GPa the alloy has b.c.c. structure. **b**, At higher pressure (above 14 GPa) it starts to transform to h.c.p. phase and at 21(1) GPa the transformation is completed **c**. No phase transformations were observed on compression to over 119(5) GPa at room temperature **d**. However, after five hours of external electrical heating at 140(10) GPa and 1,380(25) K (see also left inset) two new lines appeared at 2.494 Å and 1.762 Å belonging to the B2 structured alloy ( $a = 2.493(1)$  Å). **e**, Then, the same sample was heated for 8 h at 30(2) GPa and 1,100(10) K and the extra lines disappeared owing to back reaction of iron alloys with different concentration and only h.c.p. phase remained. NaCl was used as pressure medium (reflections marked as NaCl B1 below 30 GPa and NaCl B2 at higher pressures). Spectrum **f** and the right inset show an X-ray diffraction pattern of the sample recovered after laser-heating of Fe-10 wt% Si alloy at 105(5) GPa and 2,500(100) K (NaCl was dissolved in water). The reflections at 1.969 Å and 2.781 Å correspond to the (110) and (100) peaks of the quenched B2 FeSi phase. The lattice parameter of this phase ( $d = 2.783(2)$  Å) is just slightly lower than the lattice parameter of B2-structured FeSi ( $d = 2.7917(1)$  Å) synthesized<sup>19</sup> in multianvil experiments, indicating that the composition of the B2 phase obtained in our experiments is close to 1:1 Fe:Si mole ratio.

heating only diffraction lines of  $\epsilon$ -Fe are present (Fig. 1a). However, after heating at 2,100(100) K, silica crystallized as stishovite and new lines of wüstite appeared (Fig. 1b). The lattice parameter of iron, quenched after heating at 22–30 GPa, decreased from 2.8624(8) Å to 2.860–2.858 Å, which corresponds to a Fe-Si alloy with 3.6–4.5 wt% Si. However, heating of iron and amorphous SiO<sub>2</sub> (or re-heating of the Fe-Si alloy and stishovite) at 87(5) GPa and 3,750(200) K (for example well above iron melting temperature at corresponding pressure), as shown in Fig. 1c, resulted only in the crystallization of silica phases (CaCl<sub>2</sub>- and  $\alpha$ -PbO<sub>2</sub>- structured<sup>20</sup>). No trace of wüstite was observed in the quenched sample at high pressure and the lattice parameter of iron (2.8629(9) Å) after decompression was the same as in the starting material. Analytical transmission electron microscopy (ATEM) (see Supplementary Information) with nanometre-scale resolution of the sample after heating at 125(10) GPa and 2,500(150) K shows only the presence of a silica phase and iron (Fig. 1d). Within the analytical detection limit (0.2 wt% Si) there is no silicon in the metallic portion of the sample. In other words, we did not observe a reaction between iron and silicon at pressures of 87 and 125 GPa.

Figure 2 summarizes the results of our experiments on the Fe-SiO<sub>2</sub> reaction. At pressures between 15 GPa and 40 GPa we detected reduction of silicon by iron:



At higher pressures, above 80 GPa, we did not detect any reaction. The reason that iron and silica do not react at high pressure could be the decreasing solubility of Si in  $\epsilon$ -Fe (hexagonal close-packed (h.c.p.) structure) with increasing pressure<sup>21</sup>. Indeed, *ab initio* calculations (see Supplementary Information) predict that with increasing pressure the amount of Si that can be accommodated by h.c.p.-Fe substantially decreases and the alloy should dissociate to a mixture of silicon-poor h.c.p. Fe and the Si-rich B2 structured phase (see Supplementary Information).

Note that the theoretical calculations were done at  $T = 0$  K, whereas at high temperature entropic contribution may be important<sup>22</sup>. Therefore, theoretical predictions were tested through a series of high pressure and temperature DAC experiments on Fe-Si alloys containing 9.6(1), 5.1(1) and 4.3(4) wt% Si (later produced by equilibrating Fe with SiO<sub>2</sub> at 22 GPa and 2,473 K in multianvil apparatus, as described above). We found that all alloys behave similarly and Fig. 3 shows representative X-ray patterns obtained *in situ* at high pressure and temperature using the 5.1 wt% Si alloy as the starting material. At 300 K and pressures below 14–18 GPa all studied alloys have the b.c.c. structure (Fig. 3a). At higher pressures the alloys start to transform to the h.c.p. phase and above 20–22 GPa the transformation is completed (Fig. 3b). No further phase transformations were observed on compression to over 100 GPa (Fig. 3c) at ambient temperature, but heating promoted a transformation. Figure 3d (see also left inset in Fig. 3) shows an example of a diffraction pattern collected after 5 h of external electrical heating of the Fe-5.1 wt% Si alloy at 140(10) GPa and 1,380(25) K. Two new lines at 2.494 Å and 1.762 Å belong to the B2 structured alloy ( $a = 2.493(1)$  Å) as predicted by *ab initio* calculations (see above). When the same sample was heated for 8 h at 30(2) GPa and 1,100(10) K, the extra lines disappeared, indicating that the reaction was reversed and only the h.c.p. phase remained (Fig. 3e).

One of the samples of Fe-10 wt% Si alloy was compressed to 105(5) GPa in a NaCl pressure medium, laser-heated from both sides at 2,500(100) K. After decompression, the NaCl was carefully dissolved in water. The diffraction pattern of the recovered foil is shown in Fig. 3f (see also right inset in Fig. 3). The extra reflections at 1.969 Å and 2.781 Å correspond to the (110) and (100) peaks of quenched B2 FeSi phase. The lattice parameter of this phase (2.783(2) Å) is slightly lower than the lattice parameter of B2-structured FeSi (2.7917(1) Å) synthesized<sup>19</sup> in multianvil experiments,

indicating that composition of the B2 phase obtained in our experiments is close to 1:1 Fe:Si molar ratio.

As mentioned above, the Fe-4.3(4) wt% Si alloy, obtained by reacting SiO<sub>2</sub> and Fe at 22 GPa and 2,473 K in a multianvil apparatus, was homogeneous. However, ATEM studies of the material recovered after treatment of this alloy in a laser-heated DAC at 93(3) GPa and 2,100–2,400 K reveal a variation of silicon concentrations in different parts of the sample from ~0 to 6.6 wt%. These observations provide direct proof that the Fe–Si alloy, equilibrated with SiO<sub>2</sub> at relatively low pressures (20–30 GPa), dissociates into Si-poor and Si-rich phases at much higher pressures (about 100 GPa).

Our results on the behaviour of the Fe–Si alloys with different Si concentrations are summarized in Fig. 2b. We found that at pressures above 60 GPa and high temperatures the alloys dissociate into a mixture of h.c.p.-structured Si-poor and B2-structured Si-rich phases. Lin *et al.*<sup>17</sup> also reported dissociation of Fe–Si alloys with a Si content of more than 4 wt% on the mixture of h.c.p. and b.c.c. phases. The difference between b.c.c.- and B2-structured alloys is solely the ordering of Fe/Si atoms among the positions in the body-centred lattice—fully or partially ordered alloys are B2, and completely disordered alloys are b.c.c. Our diffraction data clearly show the (100) reflection of the B2 structure (Fig. 3d and insets), which is expected to be low in intensity (calculated intensity is 14% for a fully ordered stoichiometric FeSi compound), and could be rather difficult to detect in high pressure and temperature experiments.

The reaction between iron and silicate<sup>2,9,10,13</sup> could be a source of the iron–silicon alloy at the CMB. The density of B2 FeSi (~9.0 g cm<sup>-3</sup>) is significantly higher than the density of the mantle (~5.6 g cm<sup>-3</sup>) above the CMB and lower than the density of the core (~10.0 g cm<sup>-3</sup>) immediately below the CMB. This means that the silicon-rich alloy would accumulate at the boundary between mantle and core. *Ab initio* simulations (see Supplementary Information) and measurements on B2 FeSi recovered from multianvil experiments<sup>19</sup> show that this compound is an electric conductor (with the electrical conductivity of  $6(1) \times 10^5 \text{ S m}^{-1}$  measured at ambient conditions). Thus, anomalously high electrical conductivity at the base of Earth's mantle<sup>6</sup> could be associated with the presence of B2 FeSi.

We suggest that if silicon is present in the inner core, it should form a B2 FeSi phase (assuming that there are no further phase transitions in this material above 300 GPa and high temperatures). This implies that the Earth's inner core can be compositionally heterogeneous and contains at least two phases—the Fe-rich phase with hexagonal symmetry and the Fe–Si phase with cubic symmetry. The elastic and rheological properties of these two phases are expected to be quite different and could influence the understanding of the observed inner core anisotropy and heterogeneity<sup>5,6,11,16,17</sup>. □

Received 28 May 2002; accepted 8 January 2003; doi:10.1038/nature01422.

- Gurnis, M., Wyssession, M. E. & Knittle, E. *The Core-Mantle Boundary Region* (ed. Buffett, B. A.) (AGU, Washington DC, 1998).
- Jeanloz, R. & Williams, Q. in *Ultrahigh-Pressure Mineralogy: Physics and Chemistry of the Earth's Deep Interior* (ed. Hemley, R. J.) *Rev. Mineral.*, **37**, 241–259 (1998).
- Buffett, B. A., Garner, E. J. & Jeanloz, R. Sediments at the top of Earth's core. *Science* **290**, 1338–1342 (2000).
- Li, J. & Agee, C. B. Geochemistry of mantle–core differentiation at high pressure. *Nature* **381**, 686–689 (1996).
- Vidale, J. E. & Earle, P. S. Fine-scale heterogeneity in the Earth's inner core. *Nature* **404**, 273–275 (2001).
- Buffett, B. A. Constraints on magnetic energy and mantle conductivity from the forced nutations of the Earth. *J. Geophys. Res.* **97**, 19581–19597 (1992).
- Carnero, E. J. & Jeanloz, R. Fuzzy patches on the Earth's core-mantle boundary? *Geophys. Res. Lett.* **27**, 2777–2780 (2000).
- Gessmann, C. K., Wood, B. J., Rubie, D. C. & Kilburn, M. R. Solubility of silicon in liquid metal at high pressure: implications for the composition of the Earth's core. *Earth Planet. Sci. Lett.* **184**, 367–376 (2001).
- Knittle, E. & Jeanloz, R. Simulating the core-mantle boundary: an experimental study of high-pressure reactions between silicates and liquid iron. *Geophys. Res. Lett.* **16**, 609–612 (1989).
- Poirier, J. P., Malavergne, V. & Le Mouél, J. L. in *The Core-Mantle Boundary Region* (eds Gurnis, M., Wyssession, M. E., Knittle, E. & Buffett, B. A.) 131–137 (AGU, Washington DC, 1998).

- Steinle-Neumann, G., Stixrude, L., Cohen, R. E. & Gulseren, O. Elasticity of iron at the temperature of the Earth's inner core. *Nature* **413**, 57–60 (2001).
- Goarant, F., Guyot, F., Peyroneau, J. & Poirier, J. P. High-pressure and high-temperature reactions between silicates and liquid iron alloys in the diamond anvil cell, studied by analytical electron microscopy. *J. Geophys. Res.* **97**, 4477–4487 (1992).
- Song, X. & Ahrens, T. J. Pressure-temperature range of reactions between liquid iron in the outer core and mantle silicates. *Geophys. Res. Lett.* **21**, 153–156 (1994).
- Tschauner, O., Zerr, A., Specht, S., Rocholl, A., Boehler, R. & Palme, H. Partitioning of nickel and cobalt between silicate perovskite and metal at pressures up to 80 GPa. *Nature* **398**, 604–607 (1999).
- Dubrovinsky, L. *et al.* Chemical interaction of iron and corundum as a source of heterogeneity at the core-mantle boundary. *Nature* **412**, 527–529 (2001).
- Dubrovinsky, L. S., Saxena, S. K., Tutti, F. & Le Bihan, T. X-ray study of thermal expansion and phase transition of iron at multimegabar pressure. *Phys. Rev. Lett.* **84**, 1720–1723 (2000).
- Lin, J.-F., Heinz, D. L., Campbell, A. J., Devine, J. M. & Shen, G. Iron-silicon alloy in Earth's core? *Science* **295**, 313–315 (2002).
- Knittle, E. & Jeanloz, R. Earth's core-mantle boundary: Results of experiments at high pressures and high temperatures. *Science* **251**, 1438–1443 (1991).
- Dobson, D. P., Vocadlo, L. & Wood, I. G. A new high-pressure phase of FeSi. *Am. Mineral.* (in the press).
- Prokopenko, V. B., Dubrovinsky, L. S., Dmitriev, V. & Weber, H.-P. Raman spectroscopy and X-ray diffraction *in situ* characterization of phase transitions in cristobalite under high pressure. *J. Alloys Compounds* **327**, 87–95 (2001).
- Guyot, F. *et al.* P-V-T measurements of iron silicide (ε-FeSi)—Implications for silicate-iron interactions in the early Earth. *Eur. J. Mineral.* **9**, 277–285 (1997).
- Alfe, D., Price, G. D. & Gillan, M. J. Thermodynamic stability of Fe/O solid solution at inner-core conditions. *Geophys. Res. Lett.* **27**, 2417–2420 (2000).
- Boehler, R. Temperatures in the Earth's core from melting-point measurements of iron at high static pressures. *Nature* **363**, 534–536 (1993).
- Shen, G., Mao, H. K., Hemley, R. J. & Rievers, M. L. Melting and crystal structure of iron at high pressure. *Geophys. Res. Lett.* **25**, 373–376 (1998).

Supplementary Information accompanies the paper on Nature's website (<http://www.nature.com/nature>).

**Acknowledgements** We thank G. Herrmannsdörfer, H. Schulze, R. Eger and C. Kamella, for technical assistance. Discussion with G. D. Price allowed us to improve the manuscript. Financial support of Deutsche Forschungsgemeinschaft, the Swedish Research Council (VR), the Swedish Foundation for Strategic Research (SSF), and the EU 'Access to Research Infrastructures' Programme is acknowledged.

**Competing interests statement** The authors declare that they have no competing financial interests.

**Correspondence** and requests for materials should be addressed to L.D. (e-mail: Leonid.Dubrovinsky@uni-bayreuth.de).

## A Middle Miocene hominoid from Thailand and orangutan origins

Yaowalak Chaimanee\*, Dominique Jolly†, Mouloud Benammi‡, Paul Tafforeau§, Danielle Duzer†, Issam Moussa§ & Jean-Jacques Jaeger§

\* Paleontology Section, Geological Survey Division, Department of Mineral Resources, Bangkok -10400, Thailand

† Palynologie et Paléoenvironnements, I.S.E.M., cc 061, Place Eugene Bataillon, 34095-Montpellier, France

‡ Paleomagnetismo, Instituto de Geofísica, Universidad Nacional Autónoma de México, 04510 México DF, México

§ Paléontologie, I.S.E.M., cc 064, Université Montpellier II, Place Eugene Bataillon, 34095-Montpellier, France

The origin of orangutans has long been debated. *Sivapithecus* is considered to be the closest ancestor of orangutans because of its facial–palatal similarities<sup>1</sup>, but its dental characteristics<sup>2</sup> and postcranial skeleton<sup>2,3</sup> do not confirm this phylogenetic position. Here we report a new Middle Miocene hominoid, cf. *Lufengpithecus chiangmuanensis* n. sp. from northern Thailand. Its dental morphology relates it to the *Pongo* clade, which includes *Lufengpithecus*<sup>4,5</sup>, *Sivapithecus*<sup>2</sup>, *Gigantopithecus*<sup>6</sup>, *Ankarapithecus*<sup>7</sup> and possibly *Griphopithecus*<sup>8</sup>. Our new species